Fault friction during simulated seismic slip pulses

Christopher Harbord[1], Nicolas Brantut[1], Elena Spagnuolo[2] and Giulio Di Toro[3]

[1]Department of Earth Sciences, University College London, London, UK,

[2] Istituto Nazionale di Geofisica e Vulcanologia, Via di Vigna Murata 605, Rome, Italy,

[3] Dipartimento di Geoscienze, Università degli studi di Padova, Padua, Italy

Corresponding author: Christopher Harbord (c.harbord@ucl.ac.uk)

Key Points:

- We investigate the evolution of fault strength during realistic earthquake slip history
- The high velocity strength of carbonate built faults is compatible with flash heating at short timescales and viscous creep rheology at larger timescales.
- We document limited elastodynamic compatibility between measured fault strength and imposed slip history

Abstract

Theoretical studies predict that during earthquake rupture faults slide at non-constant slip velocity, however it is not clear which source time functions are compatible with the high velocity rheology of earthquake faults. Here we present results from high velocity friction experiments with non-constant velocity history, employing a well-known seismic source solution compatible with earthquake source kinematics. The evolution of friction in experiments shows a strong dependence on the applied slip history, and parameters relevant to the energetics of faulting scale with the impulsiveness of the applied slip function. When comparing constitutive models of strength against our experimental results we demonstrate that the evolution of fault strength is directly controlled by the temperature evolution on and off the fault. Flash heating predicts weakening behaviour at short timescales, but at larger timescales strength is better predicted by a viscous creep rheology. We use a steady-state slip pulse to test the compatibility of our strength measurements at imposed slip rate history with the stress predicted from elastodynamic equilibrium. Whilst some compatibility is observed, the strength evolution indicates that slip acceleration and deceleration might be more rapid than that imposed in our experiments.

Plain languge summary

Faults, where deformation is hosted in the upper portion of the crust, slide rapidly during earthquakes. Unfortunately how faults slip during earthquakes is not clear, with several theoretical models proposed whereby newtons second law is satisfied. Consequently we test the strength of rocks during one proposed slip history. Key observations show that strength evolution strongly depends on slip history. Temperature is also shown to be a key factor governing strength evolution, and weakening at short timescales is controlled by heating at highly stressed contacts before viscous processes accommodate deformation. Histories of realistic fault slip and compatible strength changes do not completely agree with experimental measurements. Instead we suggest that faults must accelerate and decelerate more rapidly than current models. Significantly, rapid acceleration and deceleration of faults will promote more damaging high frequency wave radiation.

1 Introduction

During earthquakes, faults weaken abruptly, and slip accelerates to velocities of the order of several metres per second (Kanamori & Brodsky, 2004; Madariaga, 2015). The exact stress and slip evolution on faults is rarely well constrained by seismological observations, which can generally only provide estimates of integrated quantities, such as average stress drop and slip, breakdown work and radiated energy (Abercrombie & Rice, 2005; Guatteri & Spudich, 2000; Kanamori & Rivera, 2006).

Fault slip can be quite complex during earthquakes, with highly variable velocity history. Models and experimental observations based on fracture mechanics exhibit the common feature of a a rapid acceleration to a peak velocity, corresponding to the passage of the rupture tip, after which slip rate decays to zero (see theoretical overview in Scholz, 2002, Section 4.2; early laboratory work by Okubo & Dieterich, 1981; Ohnaka et al., 1986, and more recent work by Rubino et al., 2017; Berman et al., 2020, among many others). Kinematic source models inverted from seismological data are often nonunique and are smoothed due to the relatively low frequency data used; specific choices have to be made for the general functional form of the slip history for fault patches, but the corresponding dynamic stress evolution (and associated derived quantities, e.g., fracture energy) strongly depends on such model choices (Guatteri & Spudich, 2000; Tinti et al., 2005). It remains unclear what source-time function would best correspond to the actual traction evolution along the fault. Tinti et al. (2005) used theoretical considerations to develop a source-time function that is compatible with elastodynamics, but it is not guaranteed that such theoretical slip function leads to traction evolution that is compatible with the rheology of the fault. Attempts have been made to verify this compatibility by comparing high velocity fault

rheology obtained in laboratory experiments with earthquake source parameters estimated from strong motion seismograms, with limited success (Chang et al., 2012; Fukuyama & Mizoguchi, 2010).

In nature, there is a feedback between the slip rate on the fault (associated with a given stress state through elastodynamic equilibrium) and the shear strength of the fault zone materials. A substantial body of work has shown that fault strength is dramatically lower at rapid deformation rates in comparison to that during slow interseismic deformation (Faulkner et al., 2011; Goldsby & Tullis, 2011; Han et al., 2007; Brantut et al., 2008; Hirose & Shimamoto, 2005; Di Toro et al., 2011). The low strength observed during rapid deformation in the laboratory can explain the propagation of ruptures in numerical models (Noda et al., 2009; Noda & Lapusta, 2013), and is quantitatively consistent with the low heat flow and shear heating estimated from borehole measurements after the 2011 Tohoku-oki earthquake (Fulton et al., 2013; Ujie et al., 2013). High velocity friction experiments have shown that sliding velocity exerts a first order control in governing the strength of faults (Goldsby & Tullis, 2011; Han et al., 2007; Di Toro et al., 2004, 2011; Tsutsumi & Shimamoto, 1997). Several physical models have been proposed to explain this weakening. Nielsen et al. (2008, 2010) developed a model of frictional melting in basic igneous rocks which showed good agreement with the experimental data of Hirose & Shimamoto (2005). The flash heating model (FH), based on frictional heating at microscale contacting asperities (Rice, 2006; Beeler et al., 2008), was successful in explaining experimental observations in crystalline felsic rocks in the absence of bulk frictional melting (Goldsby and Tullis, 2011) . More recently in carbonate rocks, grain size sensitive creep has been proposed to

explain the weakening behaviour due to the presence of nanometric grains which facilitate rapid diffusive mass transfer (Demurtas et al., 2019; De Paola et al., 2015; G. Pozzi et al., 2018).

Although velocity exerts a direct control on fault strength, a number of studies have also demonstrated the important role of fault slip history in determining strength evolution: In particular, hysteresis in the frictional strength has been systematically observed between acceleration and deceleration phases of experiments, suggesting a change in the physical state of the fault during experiments (e.g., Goldsby & Tullis, 2011; Proctor et al., 2014; Sone & Shimamoto, 2009). A number of authors have shown that this difference can be accounted for by considering the temperature rise of the fault as a state variable in FH models (Proctor et al., 2014). By controlling the thermal evolution of gouge material during high velocity friction tests Yao et al. (2016) demonstrated the key role of temperature in high velocity weakening mechanisms. In parallel, experimental data and modelling by Passelègue et al. (2014) showed that subtle effects of temperature variations on fault rock properties, such as thermal conductivity, could lead to significant effects on fault weakening.
Given that temperature evolution is directly coupled to slip history and strength through dissipation of mechanical energy, the strength evolution and the resulting dynamics of earthquakes are expected to be controlled by thermo-mechanical feedbacks.

Here, we aim to investigate the role of slip history on the the frictional response of rocks, and test the compatibility of laboratory-derived strength evolution with elastodynamics. We use a slip history that is representative of earthquake source-time functions in the form of a so-called "modified Yoffe function" as derived by Tinti et al. (2005) (see Methods section), and test a

range of initial accelerations for a fixed total slip (Figure 1). We first explore the physical mechanisms that give rise to the observed complex frictional response, and show that thermally-activated mechanisms like flash heating (near the onset of the slip) and viscous creep (at late stages) are broadly consistent with the observed frictional response. This agreement confirms the key role of temperature and temperature history in the high velocity frictional behaviour of rocks. We then analyse the compatibility of our experimental results with the traction evolution expected from a simple elastodynamic slip pulse model. The measured frictional response is not totally consistent with the model in that it shows more abrupt weakening at the onset of slip and too large re-strengthening at the termination of slip. These differences indicate that elastodynamics would likely produce either shorter slip pulses or sharper drops in slip rate at the tail end of pulses (self-healing).

2 Methodology

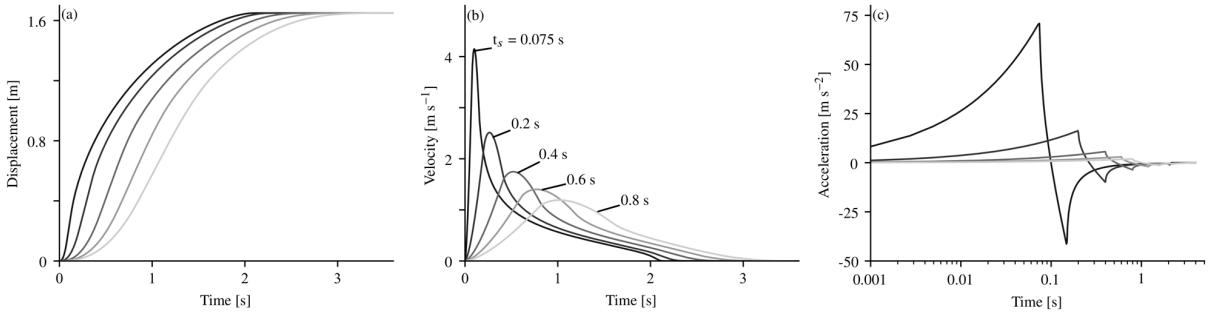

Figure 1 Yoffe function slip plotted as a function of time (a) and associated temporal derivatives, velocity (b) and acceleration (c) imposed during experiments presented in this manuscript, functions were produced following the closed form solution in Tinti et al. (2005). Here t_s is the smoothing time (see main text).

Our experiments are analogous to slip on a single point on a fault, and we therefore need to select an appropriate slip function representative of a rupture propagating through a single point in space. In practise it is not possible to define a unique solution since fault slip history depends on the interactions between fault strength and elastodynamics, however there are several

134 candidates we may choose to represent the seismic source (Kostrov, 1964; Madariaga & Nielsen,
135 2003;Tinti et al., 2005; Yoffe, 1951). The Yoffe function represents an attractive solution to
136 model slip history due to its direct compatibility with elastodynamic rupture propagation
137 (Nielsen & Madariaga, 2003; Tinti et al., 2005), and the fact that it shares similarity to slip
138 histories observed in experimental studies (Berman et al., 2020; Rubino et al., 2017). It is
139 characterised by a singular acceleration at the moving crack tip, corresponding to the crack tip
140 stress concentration, followed by an inverse square-root decay in velocity with respect to time
141 (Figure 1b). This results in slip that is approximately square root in time at a fixed observation
142 locality (Figure 1a). Given that singular acceleration is unrealistic in nature, and also not possible
143 to simulate in the laboratory, we used a regularised form of the Yoffe function presented in Tinti
144 et al. (2005). The solution is equivalent to convolving a true Yoffe function (with singular
145 acceleration) with a triangular function of time duration, $2t_s$, defined as the smoothing time.
146 Small values of the smoothing time generate more impulsive, shorter duration events i.e. faster
147 initial accelerations, and increasing t_s generates longer duration, less impulsive events (Figure
148 1). In experiments, the deconvolved timespan t_R = 2 s, and maximum displacement, U_{tot} = 1.65
149 m, were kept constant, to simulate seismic slip equivalent to a typical M_w = 7 earthquake (Wells
150 and Coppersmith, 1994). We varied t_s from 0.05 to 0.8 s, with the rise time, $t_r = t_R + 2t_s$,
151 varying between 2.1-3.6 s, which may be considered analogous to varying the rupture velocity
152 (Cochard & Madariaga, 1994).
153
154 We utilised a slow to high velocity rotary shear apparatus (SHIVA, Di Toro et al., 2010)
155 installed in the HPHT laboratory at INGV in Rome. The apparatus is capable of applying up to
156 70 kN of axial load using an electromechanical piston (Bosch-Rexroth EMC105HD), which is

157 servo controlled at a frequency of 8 kHz. A 300 kW motor servo-controlled at 16 kHz drives the
158 rotary motion up to 3000 RPM, we achieved an instantaneous acceleration of <80 m/s^2 and a
159 deceleration of <60 m/s^2 (figure 1c); outside of this range machine vibrations were too strong to
160 gather reliable data. Displacement was measured using a high resolution encoder (6297600 divs)
161 for low velocity (< 0.15 m/s) and a low resolution encoder (4000 divs) for high velocity (≥0.15
162 m/s), the encoder-derived velocity (Figure 2 grey curves) and the imposed velocity function
163 (Figure 2 black curves) show good agreement. Annular cohesive samples of Etna basalt and
164 Carrara marble of 50 mm external and 30 mm internal diameter were prepared for testing, and
165 were squared using a lathe before being ground with #80 grit prior to experimentation. All tests
166 were performed at a normal stress of 10 MPa. Torque was measured using an S-type load cell on
167 the stationary side of the apparatus and all data was logged at 12.5 kHz. A total of over 60
168 simulated slip events are presented in this study (see section ***2*** in supplementary material). In the
169 majority of experiments slip pulses were repeated using the same sample, with the normal load
170 kept constant during a minimum time period of at least 20 minutes between individual pulses.
171 Measured frictional strength was found to be highly reproducible after the first pulse (see figure
172 S1 in the supplementary material), which we interpret to indicate a consistent microstructure
173 between individual pulses.
174

3 Experimental results

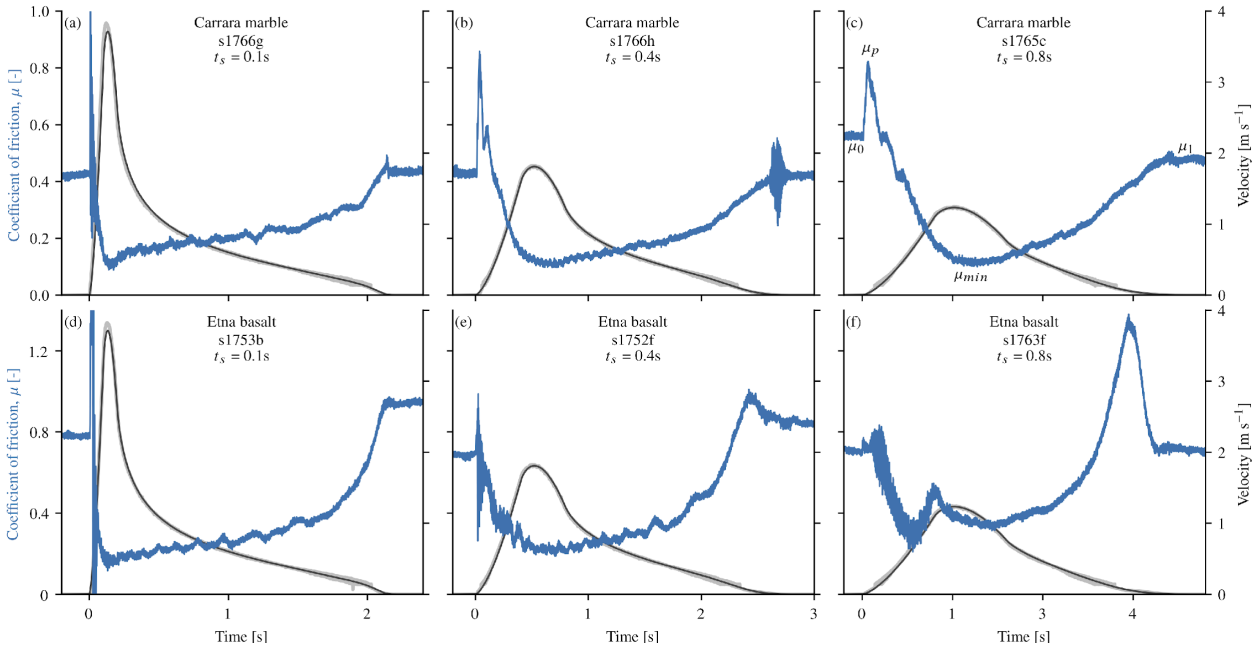

Figure 2 Frictional response of simulated faults during application of Yoffe functions of varying smoothing time. Panels a)-c) show Carrara marble with increasing values of the smoothing time from left to right (0.1 to 0.8), panels d)-f) show Etna basalt frictional response for the same slip histories as a)-c). Velocity history is shown for reference, where the thicker grey curve represents the encoder derived velocity history, and the black the imposed control signal. Panel c) is labelled according to the frictional parameters identified in the main text.

All experiments show three stages of behaviour typical of high velocity friction tests: (i) An elastic loading and slip-strengthening phase, which corresponds to an increase in friction coefficient from an initial value at zero velocity, μ_0 = 0.5–0.6 (τ_0 = 5–6 MPa), to a peak as slip rate increases, μ_p = 0.6–0.8 (τ_p= 6–8 MPa, Figures 2b and 2c); (ii) A breakdown phase past the peak in frictional strength, where friction drops from μ_p to a minimum weakened value, μ_{min}, which is generally coeval with the peak in velocity. Values of μ_{min} are typical of high velocity friction, with values around μ_{min} = 0.05–0.2 (τ_{min} =0.5–2 MPa) in marble (Figure. 2a)-c)), and μ_{min} = 0.2–0.3 (τ_{min} = 2–3 MPa) in Etna basalt (Figure 2d)-e)); (iii) A final slip restrengthening phase, where frictional strength increases steadily to a final value, μ_1, as slip rate decelerates,

corresponding to the end of the experiment. In Carrara marble the strength typically recovers to μ_1 = 0.4–0.5 (τ_1 = 4–5 MPa, Figure 1a-c), by contrast, for Etna Basalt the strength recovery can become large during deceleration, increasing with t_s (Figure 2d and f). At the largest values of t_s = 0.8s, during the restrengthening phase, the frictional strength in basalt reaches an apparent value of μ = 1–1.2 (10–12 MPa), before reducing to μ = 0.6–0.9 (6–9 MPa). In tests where this behaviour was observed the sample often failed in a brittle manner with audible cracking coeval with the peak in friction.

When comparing between experiments we observe a clear dependence between the overall frictional behaviour and the imposed smoothing time. Inspection of tests with t_s = 0.1s (with an initial acceleration rate $A = V_{max}/t_s$ ≈60m/s^2, Figure 2a) and d)) shows an almost instantaneous drop in friction, with weakening achieved on a timescale similar to t_s. As t_s is increased from 0.1 to 0.4s (Figure 2b) and e)) we observe an increase in the weakening timescale, and by extension an increase in the weakening distance. This trend continues to the largest values of t_s = 0.8 (A ≈0.7m/s^2 Figure 2c) and f)), where the weakening timescale is of similar value to t_s. In order to quantify how the smoothing time t_s influences the overall mechanical behaviour of the simulated faults, we now estimate key quantities relevant to the energetics of faulting.

211 3.1 Weakening distance

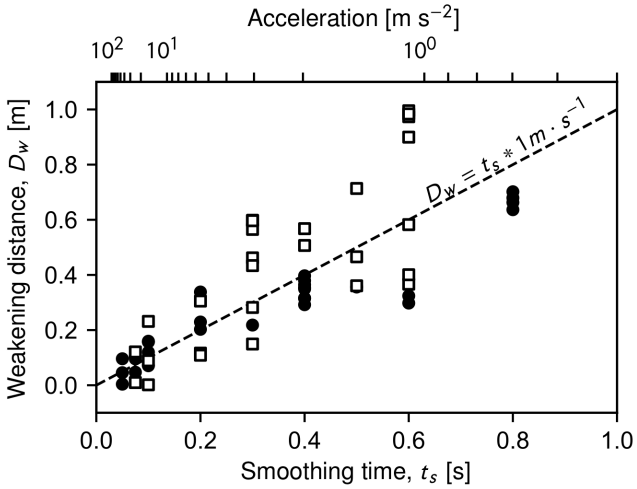

212

213 **Figure 3** Scaling of the weakening distance with the smoothing time, t_s. Filled circles represent
214 measurements derived from experiments with Carrara marble, open square symbols are Etna
215 Basalt. The top scale shows the acceleration rate, $A = V_{max}/t_s$, corresponding to the smoothing
216 timescale on the bottom x-axis defined by the relationship $A = 0.5t_s^{-1.5}$.

217 The coseismic weakening distance is an important parameter governing the propagation of
218 earthquake rupture, providing an indication of rupture efficiency (Ida, 1972). It may also provide
219 insight into the weakening mechanisms active during experiments (Hirose & Shimamoto, 2005;
220 Niemeijer et al., 2011). To estimate the weakening distance, D_w, we consider the distance at
221 which strength decreases by 95% and use the same formulation as Hirose & Shimamoto (2005)
222 and fit data using a least squares regression. Where the reduction in strength is not monotonic
223 (e.g. Figure 6f), we excluded results from the analysis. The fitted values range from 0.05–1 m
224 for the presented experiments (see supplementary table S1), and are strongly dependent on the
225 slip function applied, but are within the range of values presented in previous studies under
226 similar experimental conditions (Chang et al., 2012; Niemeijer et al., 2011). A clear trend is
227 observed between t_s and D_w (Figure 3), given that smaller values of t_s correspond to a larger
228 acceleration demonstrating an inverse dependence on the initial acceleration. For example, for
229 Carrara marble (Figure 3 filled circles), at t_s =0.05s ($A \approx 80 m/s^2$) D_w = 0.08 m, whereas for t_s =

0.8 ($A \approx 0.7 m/s^2$), the weakening distance increases to D_w =0.6 m, representing an order of magnitude change. A similar order of magnitude increase is observed in Etna basalt (Figure 3, open squares), with D_w = 0.1m at t_s =0.1s (A ≈16 m/s^2), increasing to D_w = 0.5-0.9m at t_s =0.8s (A ≈0.7m/s^2). It should be noted that values of D_w for Etna basalt become increasingly scattered as t_s increases.

3.2 Energy dissipation

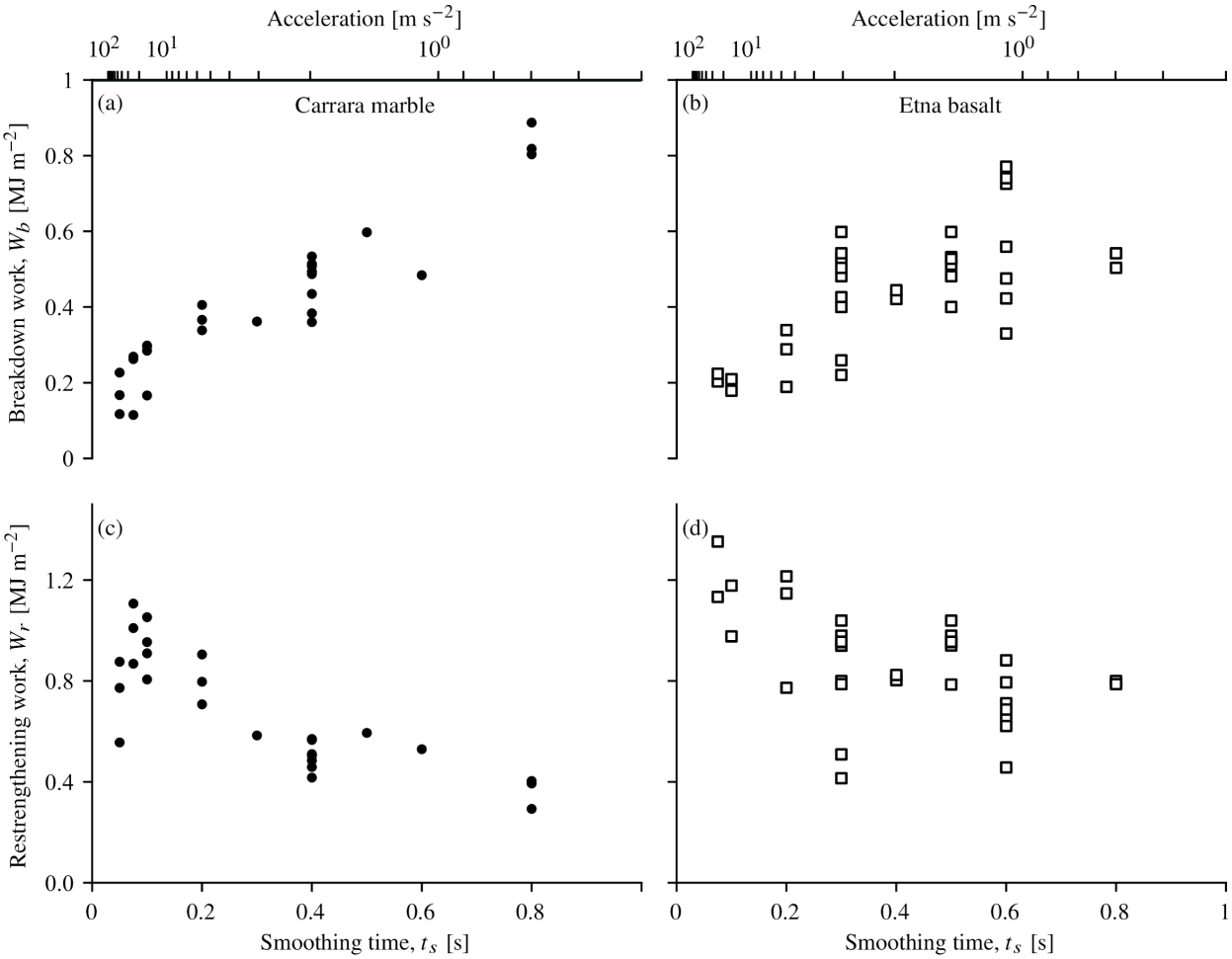

Figure 4 Partitioning of breakdown work (a) and c)) and restrengthening work (b) and d)) during simulated Yoffe pulses of varying initial acceleration rates for Carrara marble (a) and b)) and Etna Basalt (c) and d)).

241 Following previous literature, we define the breakdown work W_b [MJ m^{-2}], according to the
242 general definition of (Tinti, Fukuyama, et al., 2005),

$$W_b = \int_0^{D_{min}} [\tau(D) - \tau_{min}]\, dD, \quad (1)$$

243 Where D_{min} is the displacement when $\tau = \tau_{min}$. We also define restrengthening work, W_r, in a
244 similar manner, accordingly:

$$W_r = \int_{D_{min}}^{D_{tot}} [\tau(D) - \tau_{min}]\, dD, \quad (2)$$

245 Both of these parameters were calculated by numerical integration of the experimental shear
246 stress record with respect to slip (see Nielsen et al., 2016). This provides a quantitative estimate
247 of energy partitioning during experiments. We find that both W_b and W_r depend strongly on the
248 impulsiveness of the Yoffe function applied. Faster initial acceleration rates result in smaller
249 values of W_b and larger W_r (Figure 4). For example for t_s = 0.075s ($A \approx 80$m/s^2), W_b = 0.2
250 MJ/m^2 for both marble (Figure 4a) and basalt (Figure 4c), whereas for t_s =0.8s ($A \approx 1$m/s^2), W_b =
251 0.8 MJ/m^2 for marble and W_b = 0.9 MJ/m^2 for basalt. An inverse relationship is observed for the
252 restrengthening, with shorter deceleration time periods generally resulting in a reduction in W_r
253 (Figure 4b and c). For example when t_s = 0.8, W_r = 0.3 and 0.4 MJ/m^2 for marble and basalt
254 respectively, and for t_s = 0.1, W_r increases to 1.2 and 1.4 MJ/m^2 for marble and basalt
255 respectively. The restrengthening work is generally larger for basalt than it is for marble for a
256 given t_s or initial acceleration rate.
257

4 Driving processes of frictional evolution in the presence of complex slip velocity histories

Our results show that strong variations in slip rate induce correspondingly strong variations in frictional strength, with a rapid weakening at high slip rate and significant restrengthening as slip rate decreases. In order to identify the key driving mechanisms responsible for these variations, here we test whether such variations are captured and predicted by existing physics-based high velocity friction laws.

One key experimental observation is that the minimum strength is almost systematically occurring at the peak velocity achieved during the tests (Figure 2), which corresponds to a velocity-weakening behaviour of the rocks. Such a behaviour is typically associated with some state evolution, whereby instantaneous changes in slip rate should induce strength increase, followed by adjustments towards a lower strength state. Here, the observation of direct correlation between peak slip rate and minimum strength indicates that this state evolution occurs over time (and slip) scales much smaller than that of the change in slip rate imposed in the experiments. This is consistent with models where state was assumed to evolve over slip distances of the order of tens of microns, indeed much shorter than the slip scales measured here (e.g. Noda et al., 2009). Therefore, we primarily focus on a description of strength that excludes considerations of short-slip state evolution.

Firstly, we focus on predicting the strength of experiments using Carrara marble. We explore two commonly proposed descriptions of strength, flash heating (Goldsby & Tullis, 2011; Proctor et al., 2014; Yao et al., 2016) and grain size sensitive creep (De Paola et al., 2015; Pozzi et al., 2018; Violay et al., 2019), focussing on accurately modelling experimental boundary conditions.

Then we discuss the frictional behaviour of Etna basalt hosted faults, and provide a simple comparison to previous models of high velocity friction for melt accommodated weakening.

4.1 Flash heating

Weakening by flash heating (FH) is based on the idea that contacting asperities at the sliding interface dramatically weaken at some threshold temperature (Beeler et al., 2008; Rice, 2006). High velocity experimental data obtained using simple slip rate histories have been shown to be in general agreement with this model (Goldsby & Tullis, 2011; Proctor et al., 2014; Yao et al., 2016). The shear strength is assumed to be given by $\tau = f\sigma_n$, where the friction coefficient f behaves as

$$f = f_w + (f_0 - f_w)\frac{V}{V_w(T - T_w)}, \quad (3)$$

f_0 is the low velocity coefficient of friction, f_w the weakened coefficient of friction and V_w a critical weakening velocity that depends on the difference between the ambient fault temperature T and a critical weakening temperature T_w. The critical velocity defines a threshold at which a contacting asperity spends a portion of its lifetime above the prescribed temperature $T_w$corresponding to some weakening process, e.g., mineral decomposition (see Supplementary material section 2 for further details). Here we also explore the impact of temperature dependent asperity strength and size, which vary according to an asperity stress exponent, n.

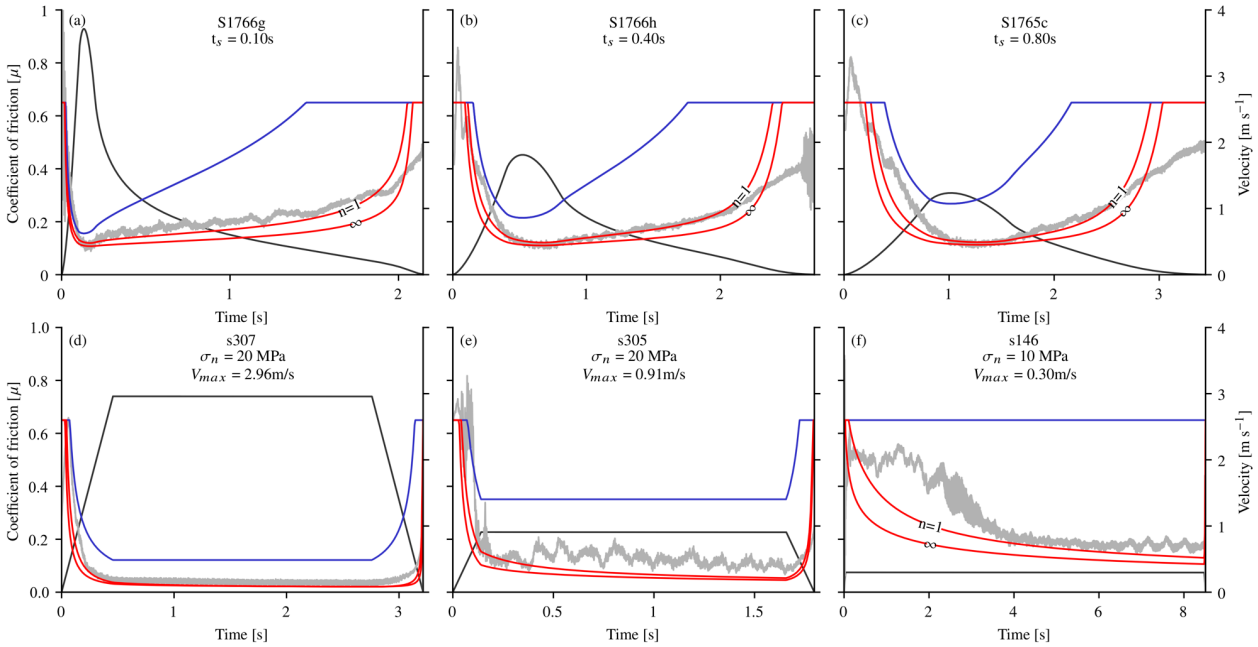

Figure 5 Flash heating models compared to experiments with Carrara marble. Blue curves represent a purely velocity dependant friction law, red curves indicate models where background temperature rise considered. Curves are labelled according to the value of the asperity stress exponent. Insets a) to c) represent experiments conducted with Yoffe slip histories, whereas d) to f) are reproduced from *Violay et al. (2013)* and were conducted with box-car slip histories. Modelled temperature histories for a) to c) are shown in figure S6 of the supplementary material.

Using the velocity histories imposed in the experiments, we first modelled fault strength with a fixed ambient temperature (Figure 5, blue curves), i.e., purely velocity-dependent strength. Comparison of this model directly with our experimental data shows that for all cases, purely velocity dependant strength is initially consistent with weakening behaviour but diverges with increasing time. When fully accounting for the rise in background temperature, modelled by introducing the bulk heat dissipation and diffusion in the rock (e.g., Proctor et al., 2014; see Supplementary Materials, Section 2), the model predictions significantly improve (Figure 5 red curves), and strength predictions generally match initial weakening behaviour during acceleration to peak velocity (t < 2s). However, the models still tend to diverge from the data at larger timescales, overestimating weakening during decelleration of the slip rate and overpredicting final restrengthening. Particularly good model agreement is found for the shortest

316 duration Yoffe slip history experiment (Figure 5a), with the strength well predicted by the
317 numerical models. The flash heating model does not match restrengthening well for any of the
318 experiments conducted with yoffe velocity history. Changes in the value of the asperity stress
319 exponent result in marginal changes to the strength predictions, when n = 1 the predicted
320 weakening is slower, and strength recovery onsets earlier, reflecting the dominance of asperity
321 strength loss in similarity to Passelègue et al. (2014).
322
323 To place the modelling results in the context of previous results we also compiled data from
324 experiments performed at similar conditions in SHIVA, where 'box-car' slip histories i.e.
325 constant acceleration to constant velocity followed by a constant deceleration to zero velocity,
326 were employed (Violay et al., 2013, 2019). Experiments run at a range of velocities are
327 reproduced and compared to models of flash heating (Figure 5d-f), and are shown to highlight
328 that all model predictions tend to overlap at high constant velocity. This overlap tends to
329 obfuscate the determination of realistic model parameters, particularly at the highest velocities, at
330 least for the range considered here. At relatively low velocity conditions differences are observed
331 between individual models (V = 0.3 m/s, Figure 5f). In agreement with experiments where slip
332 rate was given by Yoffe functions, we observe that a reasonable prediction of data can be
333 obtained when n = 1.
334
335 A consistent observation in all flash heating models is that they significantly over-predict the
336 restrengthening behaviour, and demonstrate that addition of temperature dependant asperity
337 properties does not significantly improve the prediction of strength. An improvement may be
338 yielded by accounting for a log normal distribution of asperity sizes which is a smooth function

339 of velocity (Beeler et al., 2008), which may be more representative of the geometry of
340 experimental surfaces (Candela & Brodsky, 2016).
341

342 ## 4.2 Grain size sensitive creep

343 Another proposed model of high velocity fault strength in Calcite rich faults is grain size
344 sensitive creep (GSS). This is motivated by observations of nanometric grains within
345 experimental and natural fault zones coupled to the expectation of high temperatures resulting
346 from frictional heating of the slip zone (Demurtas et al., 2019; De Paola et al., 2015; G. Pozzi et
347 al., 2018). Here we check consistency of our data with direction predictions from a GSS creep
348 law derived from deformation of fine grain calcite aggregates at high pressure temperature
349 conditions (Schmid et al., 1977):

$$\tau = \left[A^{-1}\dot{\gamma}d^{m}e^{\frac{E_a}{RT}}\right]^{\frac{1}{k}}, \quad (4)$$

350 where A is a pre-exponential factor, $\dot{\gamma}$ is the shear rate, d is the grain size, m is the grain size
351 exponent, E_a is the activation energy, R is the gas constant and k the stress exponent (see
352 Supplementary material S1, for detailed parameter values and modelling assumptions). Similarly
353 to our computations using flash heating, we fully account for the background temperature

evolution in the rock with temperature dependant thermal diffusivity.

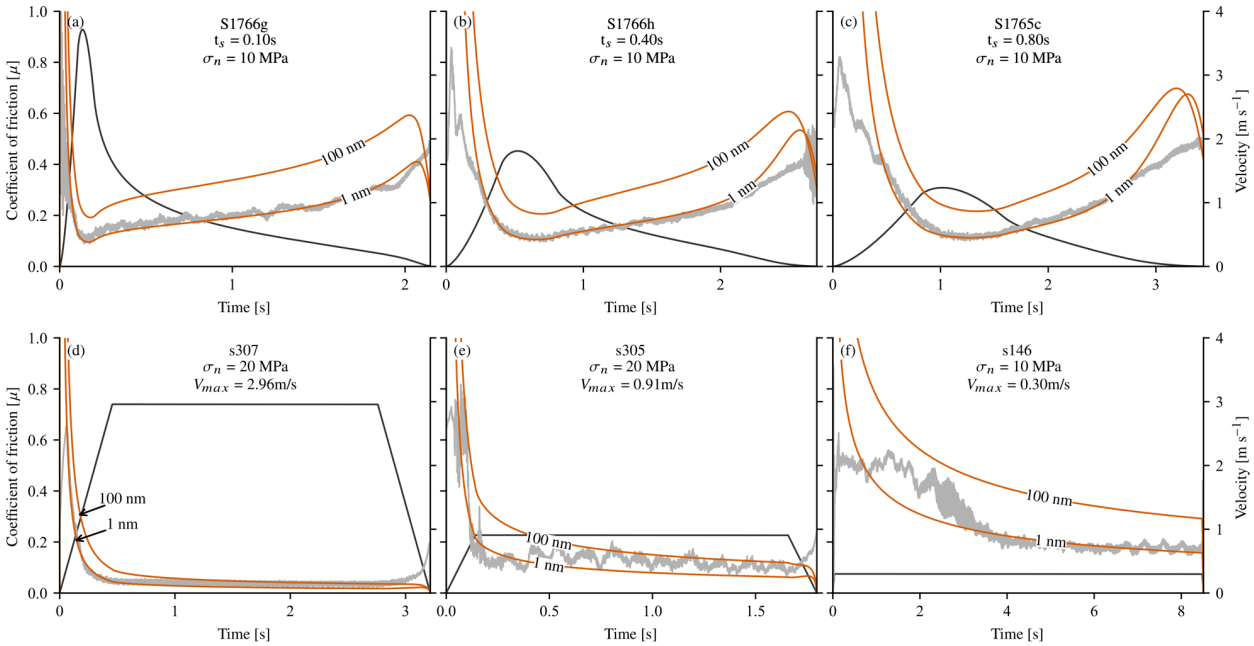

Figure 6 GSS creep models (red) compared with experimental data (grey solid lines). Curves are labelled according to grain size used in model runs. Insets a) to c) are Yoffe slip history experiments and d) to f) are reproduced experiments from *Violay et al. (2013)* with "box-car" slip histories. All experiments are the same as in figure 5. Modelled temperature histories for a) to c) are shown in figure S6 of the supplementary material.

Results from GSS models systematically overpredict the strength of faults at short timescales, and do not predict the initial weakening for all values of t_s (Figure 6a, b and c). However, from the late stages of weakening, up to the later stages of restrengthening we observe a good prediction of strength evolution. When t_s = 0.1 s the restrengthening is well matched, however for larger values of t_s = 0.4 s and 0.8 s, GSS models systematically predict a faster restrengthening rate during the final deceleration period than experiments. At cessation of slip, as velocity decreases below ~1 mm/s, the model predicts a complete loss of strength at all conditions consistently with the GSS flow law (Figure 6a, b and c). The prediction of zero strength when compared to the experimental data suggests that GSS may no longer accommodate deformation during the final stages of slip. A grain size of 1 nm is systematically

371 required to predict the strength of faults with Yoffe velocity history (Figure 6 a-c). Again, for
372 comparison purposes, results are shown from Violay et al., (2013) and Violay et al., (2019). With
373 GSS models a reduced degree of convergence is observed at constant velocity, although the same
374 grain sizes show a generally similar behaviour at large timescales where sliding velocity is high
375 (V >= 1 m/s, Figure 6d and e). A reasonable agreement between models and data is observed for
376 a box-car slip history at velocity of 0.3 m/s (fig 6f), identifying the wider applicability of the
377 creep model across the range of sliding velocities. Again, 1 nm grain sizes are required to
378 accurately predict the strength of experiments conducted with a box car velocity history at low
379 velocity, low normal stress conditions (Figure 6f), however use of a 100 nm grain size shows
380 good agreement with the higher velocity experiments (fig 6d and e).
381
382 The nanometric grain size required to match fault strength is probably unrealistic (De Paola et
383 al., 2015; Pozzi et al., 2018; Pozzi et al., 2021; Violay et al., 2013). However, this could be
384 remedied by using a modified, much larger value for the preexponential factor in Equation 4;
385 here, we decided to use an empirical estimate from an exisiting dataset obtained at low strain
386 rate, but several physical phenomena might dramatically change that value. Pre-exponential
387 factors include contributions from grain boundary geometry (thickness and roughness) and grain
388 boundary self-diffusion (Poirier, 1985). It is possible that the fault microstructure during initial
389 weakening, which has been demonstrated to result from dislocation avalanches (Spagnuolo et al.,
390 2015), may result in anhedral nanograins with larger grain boundary aspect ratio when compared
391 to the final microstructure which is likely to have annealed during cooling of the fault. Raj &
392 Ashby (1971) demonstrated that increases in the aspect ratio of contacting grain boundaries

increases the self-diffusion coefficient, resulting in reduced yield stress, which may preclude the need for unrealistically small grain sizes.

It is also important to consider that if flash processes occur during initial fault weakening, temperature may be locally higher than predicted from GSS models. An initial flux of heat resulting from asperity-scale processes may be sustained throughout the test duration (Aretusini et al., 2021), which would allow larger grain sizes to give quantitative agreement with the experimental data. We also note that in Violay et al. (2019) the authors were able to match the final fault restrengthening of the data presented in Figure 6d) by accounting for heat loss in two dimensions.

4.3 The importance of accurate temperature history

Both the flash heating and grain size sensitive creep models demonstrate the importance of incorporating temperature history into the models, and shows that it is important to consider appropriate thermal properties in model boundary conditions. This point was first highlighted by Yao et al. (2016) where experiments were conducted using sample holders of varying thermal diffusivity, demonstrating that varying temperature histories give differing strength evolutions. Here we further test this hypothesis by comparing the output of both FH and GSS models by using previously published calcite gouge experimental data obtained with a range of sample holders of varying diffusivity (Cverna, 2002). We consider, in order of increasing thermal diffusivity, grade 4 Titanium alloy (Ti90Al6V4, Pozzi et al., 2018), AISI 316 stainless steel (De Paola et al., 2015) and tungsten carbide (Smith et al., 2013). We approximate each experimental geometry as closely as possible in 1D, with the principal slip zone localised asymmetrically on

the boundary between the gouge layer and the sample holder with appropriate thermal diffusivity (De Paola et al., 2015; Pozzi et al., 2018a; Smith et al., 2013, see supplementary material S1).

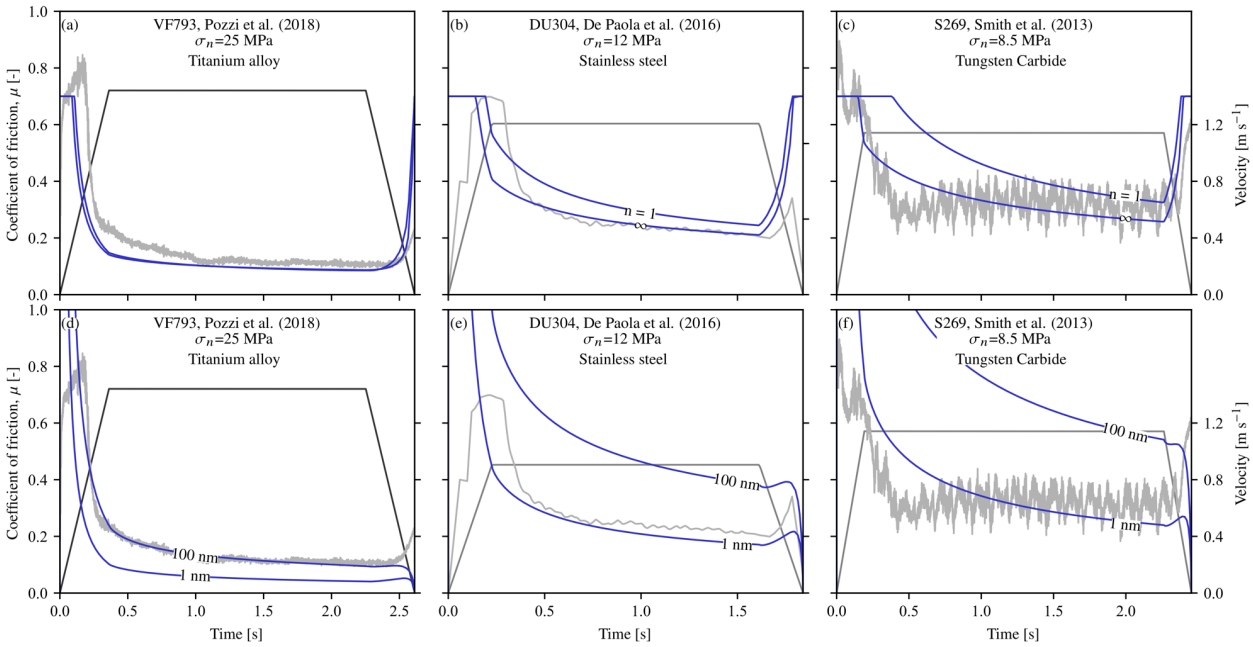

Figure 7 Effects of varying thermal diffusivity in full thickness models (blue curves) with realistic sample boundary conditions compared to previously published experimental data (grey curves). Panels a) to c) are modelled using the flash heating model described in previous discussion, with fixed thermal diffusivity with curves labelled according to the asperity stress exponent used. Panels d) to f) show the same experimental data, however this time using the GSS model defined in the previous discussion with fixed thermal diffusivity, curves are labelled according to the grain size used in the model prediction. Thermal diffusivity increases from the left to right of the figure.

For both rheological models we observe that for increasing thermal diffusivity, the fault strength predictions increase, consistently with experimental observations (Figure 7). Generally FH does not predict the initial weakening behaviour, predicting faster weakening in Titanium alloy (Figure 7a) and Stainless steel (Figure 7b), and less abrupt weakening for tungsten carbide (Figure 7c). The differences in model predictions and experimental data may result from strain localisation and grain crushing that occurs during early stages of slip in gouges (Logan et al.,

1992). During steady state sliding conditions the FH models are able to predict strength evolution with reasonable success, and in particular predict a slow progressive weakening with slip resulting from a progressive temperature rise, sharing similarities to the experimental data (Figure 7a, b and c). The restrengthening is systematically over predicted by the flash heating models, similarly to the results shown in the previous section.

Initial weakening is predicted comparatively better for GSS than it is for FH. Similarly to FH, the GSS models also predict progressive weakening observed during constant velocity conditions (e.g. Figure 7e). The restrengthening rate predicted by models is slower than observed in experiments, and consistently with previous discussion of GSS models, strength falls to zero as slip arrests. Generally we observe that the best predictions of fault strength for the gouge experiments are obtained for the previously used parameter set, except at the highest normal stress conditions. Given that we may use the same parameters in the constitutive friction law (FH or GSS), it suggests that the key variable is the bulk temperature evolution. In short, reconciling these individual experimental observations is difficult without carefully considering model boundary conditions and demonstrates that it is of fundamental importance to accurately capture on and off-fault thermal boundary conditions accurately, confirming the conclusions of Yao et al. (2016).

4.4 Interplay of weakening mechanisms

Flash heating predictions are better at shorter timescales, whereas longer timescales demonstrate a better prediction by GSS models. In fact all FH models significantly over predict the final strengthening behaviour. Taken together these observations suggest that multiple weakening

meachanisms may operate simultaneously during experiments with a potential transition in dominance. At early stages when the bulk fault temperature is low, and GSS is not efficient, behaviour will be dominated by asperity scale flash heating processes leading to bulk heating of the principle slip zone. However as slip and fault temperature increases, GSS deformation becomes increasingly favourable. This transition has been previously proposed by Pozzi et al. (2018) and De Paola et al. (2015), however they did not explicitly consider FH at early stages of slip, suggesting instead that the transition is simply from cataclastic processes to GSS. If FH was active during early stages of slip it is possible that the high contact temperatures during weakening may be sustained during later stages of the experiment and deformation could be accommodated by larger grain sizes. Effectively the two constitutive equations define a threshold temperature at which fault strength approaches a residual strength. In the case of FH this is given by the temperature at which a generic weakening process occurs (which could be GSS), whereas for GSS it defines the temperature at which efficient diffusive mass transfer occurs, in both the governing state variable is fault temperature.

4.5 Weakening and restrengthening in basalt

Weakening of basaltic experimental faults is facilitated by frictional melting, which leads to the formation of a hot low viscosity melt layer (Hirose & Shimamoto, 2005; Niemeijer et al., 2011; Rempel & Weaver, 2008; Violay et al., 2019, see videos S3 and S4). Modelling of weakening accommodated by melting has previously addressed by Nielsen et al. (2008) and Rempel & Weaver (2008) who explicitly considered the effects of the effects of progressive melt formation during high velocity sliding. Melting of rock during frictional sliding at high velocity can be shown to result in a complex 2-stage weakening behaviour, reflecting the degree of melt layer

483 formation, with the presence of initially patchy melt leading to strengthening, followed by
484 secondary weakening due to the formation of a continuous meltlayer (Del Gaudio et al., 2009;
485 Hirose & Shimamoto, 2005; Rempel & Weaver, 2008). This is evident in our experiments with
486 slower initial acceleration rates (e.g. t_s = 0.8s, Figure 2f). When acceleration is sufficiently high,
487 then weakening is monotonic (Figure 2d), consistently with Del Gaudio et al. (2009).

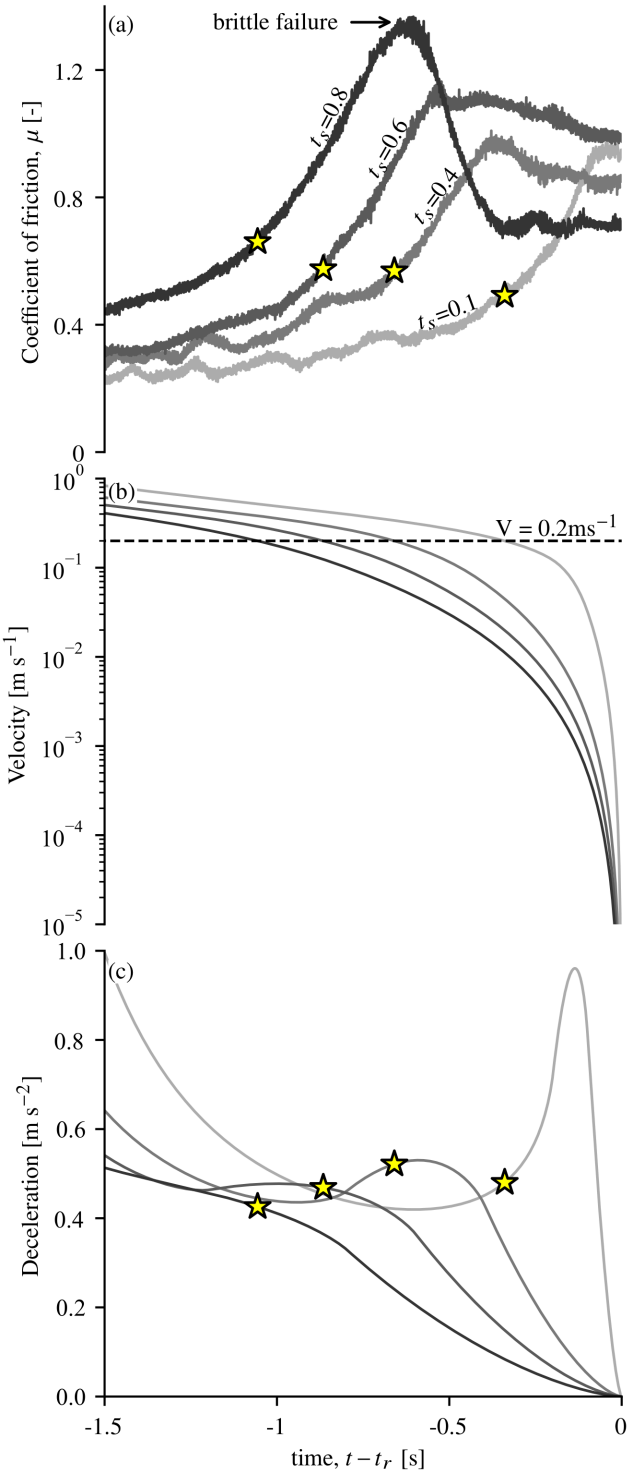

Figure 8 Restrengthening phase in basalt, illustrating the relationship between final deceleration and restrengthening behaviour in Etna basalt. Curves are coloured according to the smoothing time, stars indicate where slip velocity falls below a critical rate, W (analogous to V_w) as defined in Nielsen et al. (2008).

493 Turning attention now to the restrengthening phase of basalt experiments, we observe a clear
494 relationship between the final deceleration rate and restrengthening behaviour (Figure 8). Where
495 final deceleration is sufficiently rapid, t_s = 0.1 s, then no strength overshoot is observed, and
496 friction monotonically increases up to the end of the experiment, with μ_1 = 0.9. As the
497 deceleration rate is decreased as a result of increasing t_s, we observe increasing amounts of
498 strength overshoot, and faster restrengthening rates. For the largest value of smoothing time (t_s=
499 0.8s), the strength overshoot is considerable, with a coefficient of friction close to 1.4 (Figure
500 8a), almost twice the initial value of μ = 0.7. Such large increases in strength suggest melt
501 solidification and cohesion of the fault, and where large overshoot was observed cracking was
502 heard, identifying that the melt solidified and failed in a brittle manner (see video S4). In the
503 limit of adiabatic instantaneous deceleration, the fault stress would instantaneously drop as a
504 result of the Arrhenius dependance of melt viscosity (Giordano et al., 2008). However where
505 deceleration is slow, heat diffusion dominates and significant strengthening occurs due to melt
506 solidification. According to Nielsen et al. (2008) frictional melt is expected to form or be
507 sustained above a crictical velocity of approximately 0.2 m s^{-1} for Etna basalt. A velocity of 0.2
508 m s^{-1} agrees well with the onset of restrengthening in our experiments, with the magnitude
509 correlating well with the timescale faults spend sliding at velocities less than this rate (Figure
510 8a).

511 **5 Are laboratory friction data compatible with elastodynamics?**

512

513 In the previous section we analysed the potential driving processes that produce the observed
514 evolution of friction in response to an imposed slip history. In nature, during an earthquake, the
515 evolution of frictional strength feeds back into the slip history due to elastodynamic stress

redistribution and the requirement of stress equilibrium. To illustrate this, let us consider the elastic stress field associated with anti-plane slip along a 1d linear fault trace:

$$\tau(x,t) = -\frac{G}{2c_s}V(x,t) + \int_{\Sigma}\int_{0}^{t} K(x-\xi;t-t')V(\xi,t)dt'dV + \tau_b, \quad (5)$$

where G is the shear modulus, c_s is the shear wave speed, V the on fault particle velocity, x is the position along the fault, and K the dynamic load associated to points on the fault that are still slipping.

The dynamic load term in equation 5 is composed of the integrated slip history across the entire span of the rupturing fault. Waves radiated from other points on the fault results in dynamic loading which modifies slip-stress history, typically resulting in a heterogeneous slip history on the fault plane. In addition, the transfer of stress, wave propagation and rupture velocity depends also on the geometry of the rupturing fault, so that the typical non-planar geometry of natural faults will also influence the slip-stress history (e.g., Romanet et al., 2020). Therefore, slip history at a point on a fault is highly non-unique and depends on the entire integrated rupture history, and in practise there is no unique test of elastodynamic compatibility.

In order to test the compatibility of our experiments with elastodynamics, we must make several simplifying assumptions. To do this we consider a steady-state slip pulse model, where both the rupture velocity and source duration are constant. In this case the elastodynamic equilibrium in anti-plane geometry can be simplified to

$$\tau(x) = \tau_b + \frac{G^*}{2\pi V_r}\int_{0}^{L}\frac{V(s)}{s-x}ds, \quad (6)$$

535 where τ_b is the ambient shear stress, L the pulse length (equivalent to the product of rupture
536 velocity and total rise time), G^* is the shear modulus multiplied by a function of the ratio of
537 rupture speed V_r and shear wave speed. Equation (6) gives the dynamic elastic stress produced by
538 the slip rate distribution along the pulse. In our experiments, the slip rate is imposed as a function
539 of time. Here we consider that this slip rate evolution represents the relative motion of two
540 opposing points along a steadily propagating pulse. Choosing a constant rupture speed, we first
541 compute the elastic stress by direct integration of (6), and compare it to the measured
542 experimental strength (for details of methodology see Viesca & Garagash (2018) and
543 supplementary material S3). Since strength should be equal to stress during slip to satisfy
544 mechanical equilibrium, any deviations between predicted stress and measured strength would
545 indicate inconsistency between the rheological behaviour of the fault and our choice of imposed
546 slip rate.
547

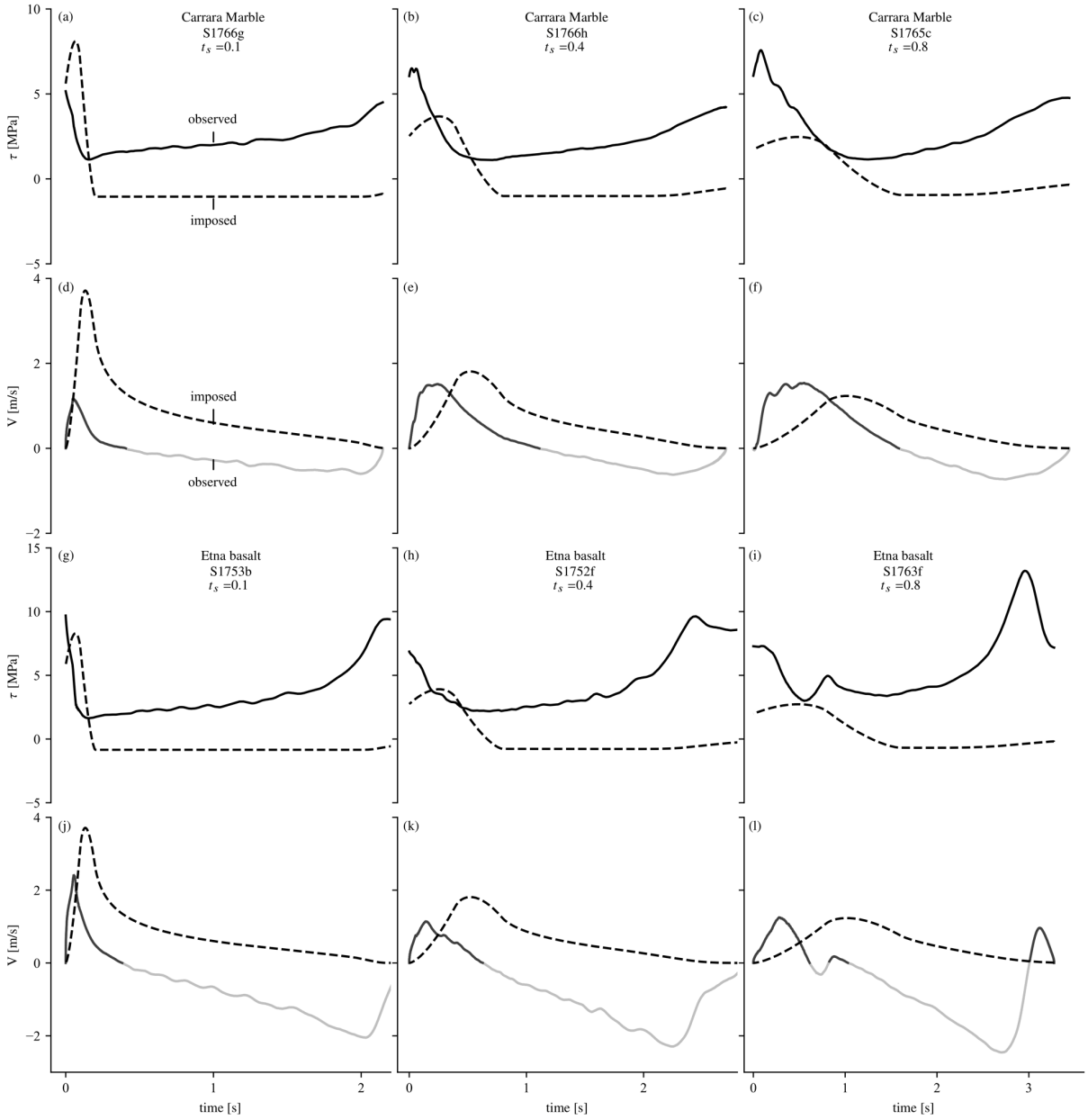

Figure 9 Experimental data compared to elastodynamic solution using steady state pulse model of rupture propagation. Dashed shear stress curves indicate solutions compatible with the imposed velocity history during an experiment, and overlay smoothed experimental data (solid curves, labelled as observed in a)). The solid velocity history is that which is predicted from the measured evolution of shear stress (traction) during an experiment, lines are coloured grey where $V < 0$ m/s.

The stress predicted by imposing the velocity history is only qualitatively compatible with the overall evolution of strength during tests: there is an initial weakening phase, with strength

558 decreasing until sliding occurs at constant stress after which the stress increases during final slip
559 deceleration, although the precise magnitudes and timings do not agree. In particular, the
560 predicted final stress increase occurs later than in experimental observations, with a
561 comparatively smaller magnitude.
562
563 We can also use our strength measurements to predict what would be the slip rate evolution
564 along a hypothetical pulse, i.e., to determine $V(x)$ based on $\tau(x)$ in (6), assuming this time that
565 strength is equal to elastic stress, and compare this slip rate to the originally imposed
566 experimental slip rate. By imposing zero slip velocity before and after the rupture interval, we
567 also constrain the background stress τ_b for our hypothetical pulse (see appendix section 3 for
568 details). While there are encouraging similarities between model and observation, the predicted
569 slip rate is quantitatively inconsistent with the imposed one. In particular, the final increase in
570 stress measured in experiments results in back-slip where velocity is negative (e.g. Figure 9k).
571 The prediction of back-slip is not realistic and would not occur during spontaneous rupture.
572
573 Overall, the experimental data show limited compatibility with our simple slip pulse model.
574 Considering that the strength is mostly controlled by slip rate (with short state evolution
575 distances) and temperature, we expect that slip rate and strength evolution that are compatible
576 with elastodynamics would involve abrupt changes in slip rate together with rapid strength
577 changes, both at the rupture tip and at the cessation of slip. For instance, in Carrara marble (e.g.
578 Figure 9a and d, sample S1766g), imposing a relatively constant slip rate after initial acceleration
579 will lead to slowly decreasing strength (due to temperature rise), which is likely to eliminate the
580 possibility of back-slip. Then, an abrupt velocity drop might be consistent with an increase in

strength above the elastic stress, producing spontaneous slip arrest. Our observations of peak weakening coeval with peak velocity is partially at odds with elastodynamic models (Tinti, Fukuyama, et al., 2005; Tinti, Spudich, et al., 2005), where peak weakening occurs after peak velocity during slip rate deceleration. In contrast, slip functions and associated elastic stress in Mikumo et al. (2003) show peak weakening coeval with peak slip velocity, after which slip rate drops to a relatively constant value, which is qualitatively consistent with our previous discussion.

The results on Etna basalt further support the requirement for rapid final slip deceleration as the strength increases quickly during melt solidification, resulting in a highly unrealistic minimum compatible slip rate of ≈ –2 m/s (Figure 9l), consistent with the notion of melt 'fusion' during high velocity sliding (Fialko & Khazan, 2005).

6 Conclusions

In this work we document results from high velocity friction experiments imposing a realistic source time history, in order to investigate how fault strength evolves during earthquakes. Simple first order observations show that the weakening distance and breakdown work are inversely dependent on the initial acceleration rate. Experimental results combined with modelling demonstrate that the high velocity strength of faults during variable velocity strongly depends on prior sliding history and temperature evolution. Carbonate built fault strength can be accurately predicted by flash heating at small time scales and grain size sensitive creep at larger timescales, provided that model boundary conditions are faithful to experimental conditions. Where flash heating is utilised to model the fault strength of carbonate built faults, then final restrengthening is always over predicted. In the case that a creep constitutive law is used there are some

significant differences between requisite grain sizes for accurate strength predictions and observed grain sizes from microstructural observations (De Paola et al., 2015; Pozzi et al., 2018; Pozzi et al., 2021). This discrepancy remains unresolved, and might be due to incorrect assumptions about our choice of deformation mechanism or the estimated temperature. However, the remarkable agreement between model predictions and observations indicates that thermally activated viscous flow laws are good candidates for the rheology of faults at high velocity.

These results provide an important validation of constitutive laws of frictional strength under non-constant velocity histories, justifying their use in coupled elastodynamic models, when the temperature rise of the fault is considered (e.g., Brantut & Viesca, 2017; Noda et al., 2009).

In our experiments, we imposed a slip rate history and measured the resulting strength. In nature, there is a feedback between strength and slip rate evolution due to elastodynamic stress redistribution. We tested the consistency of our experimental data with a simple elastodynamic model, and found discrepancies, i.e., the measured strength does not match the predicted elastic stress associated with the imposed slip. It is likely that the rheology of the fault gives rise to velocity changes (acceleration and deceleration) more abrupt than in our imposed source-time functions.

Acknowledgments, Samples, and Data

This project has received funding from the European Research Council (ERC) under the European Union's Horizon 2020 research and innovation programme (grant agreement n° 804685/"RockDEaF" and under the European Community's Seventh Framework Programme (grant agreement n° 614705/"NOFEAR"). The authours would like to acknowledge Giacomo Pozzi and an anonymous reviewer and discussions with Massimo Cocco and Elisa Tinti.

All raw experimental data is available at https://zenodo.org/record/4644245

References

Abercrombie, R. E., & Rice, J. R. (2005). Can observations of earthquake scaling constrain slip weakening? *Geophysical Journal International*, *162*(2), 406–424. https://doi.org/10.1111/j.1365-246X.2005.02579.x

Aretusini, S., Núñez-Cascajero, A., Spagnuolo, E., Tapetado, A., Vázquez, C., & Di Toro, G. (2021). Fast and Localized Temperature Measurements During Simulated Earthquakes in Carbonate Rocks. *Geophysical Research Letters*, *48*(9). https://doi.org/10.1029/2020GL091856

Beeler, N. M., Tullis, T. E., & Goldsby, D. L. (2008). Constitutive relationships and physical basis of fault strength due to flash heating. *Journal of Geophysical Research: Solid Earth*, *113*(1), 1–12. https://doi.org/10.1029/2007JB004988

Berman, N., Cohen, G., & Fineberg, J. (2020). Dynamics and properties of the cohesive zone in rapid fracture and friction. *Physical Review Letters*, *125*(12), 125503. https://doi.org/10.1103/PhysRevLett.125.125503

Brantut, N., & Viesca, R. C. (2017). The fracture energy of ruptures driven by flash heating. *Geophysical Research Letters*, *44*(13), 6718–6725. https://doi.org/10.1002/2017GL074110

Candela, T., & Brodsky, E. E. (2016). The minimum scale of grooving on faults. *Geology*, *44*(8), 603–606. https://doi.org/10.1130/G37934.1

Chang, J. C., Lockner, D. A., & Reches, Z. (2012). Rapid acceleration leads to rapid weakening in earthquake-like laboratory experiments. *Science*, *338*(6103), 101–105. https://doi.org/10.1126/science.1221195

Cochard, A., & Madariaga, R. (1994). Dynamic faulting under rate-dependent friction. *Pure and Applied Geophysics PAGEOPH*, *142*(3–4), 419–445. https://doi.org/10.1007/BF00876049

Cverna, F. (2002). *ASM Ready Reference: Thermal Properties of Metals*. ASM International. Retrieved from https://app.knovel.com/hotlink/toc/id:kpASMRRTP1/asm-ready-reference-thermal/asm-ready-reference-thermal

655 Demurtas, M., Smith, S. A. F., Prior, D. J., Brenker, F. E., & Di Toro, G. (2019). Grain Size
656 Sensitive Creep During Simulated Seismic Slip in Nanogranular Fault Gouges: Constraints
657 From Transmission Kikuchi Diffraction (TKD). *Journal of Geophysical Research: Solid*
658 *Earth*, *124*(10), 10197–10209. https://doi.org/10.1029/2019JB018071

659 Faulkner, D. R., Mitchell, T. M., Behnsen, J., Hirose, T., & Shimamoto, T. (2011). Stuck in the
660 mud? Earthquake nucleation and propagation through accretionary forearcs. *Geophysical*
661 *Research Letters*, *38*(18). https://doi.org/10.1029/2011GL048552

662 Fialko, Y., & Khazan, Y. (2005). Fusion by earthquake fault friction: Stick or slip. *Journal of*
663 *Geophysical Research: Solid Earth*, *110*(12), 1–15. https://doi.org/10.1029/2005JB003869

664 Fukuyama, E., & Mizoguchi, K. (2010). Constitutive parameters for earthquake rupture
665 dynamics based on high-velocity friction tests with variable sliprate. *International Journal*
666 *of Fracture*, *163*(1–2), 15–26. https://doi.org/10.1007/s10704-009-9417-5

667 Del Gaudio, P., Di Toro, G., Han, R., Hirose, T., Nielsen, S., Shimamoto, T., & Cavallo, A.
668 (2009). Frictional melting of peridotite and seismic slip. *Journal of Geophysical Research*,
669 *114*(B6). https://doi.org/10.1029/2008jb005990

670 Giordano, D., Potuzak, M., Romano, C., Dingwell, D. B., & Nowak, M. (2008). Viscosity and
671 glass transition temperature of hydrous melts in the system CaAl2Si2O8-CaMgSi2O6.
672 *Chemical Geology*, *256*(3–4), 203–215. https://doi.org/10.1016/j.chemgeo.2008.06.027

673 Goldsby, D. L., & Tullis, T. E. (2011). Flash Heating Leads to Low Frictional Strength of
674 Crustal Rocks at Earthquake Slip Rates. *Science*, *334*(6053), 216–218.
675 https://doi.org/10.1126/science.1207902

676 Guatteri, M., & Spudich, P. (2000). What can strong-motion data tell us about slip-weakening
677 fault-friction laws? *Bulletin of the Seismological Society of America*, *90*(1), 98–116.
678 https://doi.org/10.1785/0119990053

679 Han, R., Shimamoto, T., Hirose, T., Ree, J.-H., & Ando, J. -i. (2007). Ultralow Friction of
680 Carbonate Faults Caused by Thermal Decomposition. *Science*, *316*(5826), 878–881.
681 https://doi.org/10.1126/science.1139763

682 Hirose, T., & Shimamoto, T. (2005). Growth of molten zone as a mechanism of slip weakening
683 of simulated faults in gabbro during frictional melting. *Journal of Geophysical Research:*
684 *Solid Earth*, *110*(5), 1–18. https://doi.org/10.1029/2004JB003207

685 Ida, Y. (1972). Cohesive force across the tip of a longitudinal-shear crack and Griffith's specific
686 surface energy. *Journal of Geophysical Research*, *77*(20), 3796–3805.
687 https://doi.org/10.1029/JB077i020p03796

688 Kanamori, H., & Brodsky, E. E. (2004). The physics of earthquakes. *Reports on Progress in*
689 *Physics*, *67*(8), 1429–1496. https://doi.org/10.1088/0034-4885/67/8/R03

690 Kanamori, H., & Rivera, L. (2006). Energy partitioning during an earthquake. *Geophysical*
691 *Monograph Series*, *170*, 3–13. https://doi.org/10.1029/170GM03

Kostrov, B. V. (1964). Selfsimilar problems of propagation of shear cracks. *PMM*, *28*(5), 889–898.

Logan, J. M., Dengo, C. A., Higgs, N. G., & Wang, Z. Z. (1992). *Fabrics of experimental fault zones: Their development and relationship to mechanical behavior*. *Fault Mechanics and Transport Properties of Rocks* (Vol. 1).

Madariaga, R. (2015). *Seismic Source Theory*. *Treatise on Geophysics: Second Edition* (Vol. 4). Elsevier B.V. https://doi.org/10.1016/B978-0-444-53802-4.00070-1

Mikumo, T., Olsen, K. B., Fukuyama, E., & Yagi, Y. (2003). Stress-breakdown time and slip-weakening distance inferred from slip-velocity functions on earthquake faults. *Bulletin of the Seismological Society of America*, *93*(1), 264–282. https://doi.org/10.1785/0120020082

Nielsen, S., & Madariaga, R. (2003). On the Self-Healing Fracture Mode. *Bulletin of the Seismological Society of America*, *93*(6), 2375–2388. https://doi.org/10.1785/0120020090

Nielsen, S., Di Toro, G., Hirose, T., & Shimamoto, T. (2008). Frictional melt and seismic slip. *Journal of Geophysical Research: Solid Earth*, *113*(1), 1–20. https://doi.org/10.1029/2007JB005122

Nielsen, S. B., Spagnuolo, E., Smith, S. A. F., Violay, M., Di Toro, G., & Bistacchi, A. (2016). Scaling in natural and laboratory earthquakes. *Geophysical Research Letters*, *43*(4), 1504–1510. https://doi.org/10.1002/2015GL067490

Niemeijer, A., Di Toro, G., Nielsen, S., & Di Felice, F. (2011). Frictional melting of gabbro under extreme experimental conditions of normal stress, acceleration, and sliding velocity. *Journal of Geophysical Research: Solid Earth*, *116*(7), 1–18. https://doi.org/10.1029/2010JB008181

Noda, H., & Lapusta, N. (2013). Stable creeping fault segments can become destructive as a result of dynamic weakening. *Nature*, *493*(7433), 518–521. https://doi.org/10.1038/nature11703

Noda, H., Dunham, E. M., & Rice, J. R. (2009). Earthquake ruptures with thermal weakening and the operation of major faults at low overall stress levels. *Journal of Geophysical Research: Solid Earth*, *114*(7), 1–27. https://doi.org/10.1029/2008JB006143

Ohnaka, M., Kuwahara, Y., Yamamoto, K., & Hirasawa, T. (1986). Dynamic breakdown processes and the generating mechanism for high frequency radiation during stick-slip instabilities. In *Geophysical Monograph Series* (Vol. 37).

Okubo, P. G., & Dieterich, J. H. (1981). Fracture energy of stick-slip events in a large scale biaxial experiment. *Geophysical Research Letters*, *8*(8), 887–890. https://doi.org/10.1029/GL008i008p00887

De Paola, N., Holdsworth, R. E., Viti, C., Collettini, C., & Bullock, R. J. (2015). Can grain size sensitive flow lubricate faults during the initial stages of earthquake propagation? *Earth and Planetary Science Letters*, *431*, 48–58. https://doi.org/10.1063/1.2756072

729 Passelègue, F. X., Goldsby, D. L., & Fabbri, O. (2014). The influence of ambient fault
730 temperature on flash-heating phenomena. *Geophysical Research Letters*, *41*(3), 828–835.
731 https://doi.org/10.1002/2013GL058374

732 Poirier, J. P. (1985). *Creep of crystals*. *Physics of the Earth and Planetary Interiors* (Vol. 41).
733 https://doi.org/10.1016/0031-9201(85)90106-2

734 Pozzi, G., De Paola, N., Nielsen, S. B., Holdsworth, R. E., & Bowen, L. (2018). A new
735 interpretation for the nature and significance of mirror-like surfaces in experimental
736 carbonate-hosted seismic faults. *Geology*, *46*(7), 583–586.
737 https://doi.org/10.1130/G40197.1

738 Pozzi, Giacomo, De Paola, N., Nielsen, S. B., Holdsworth, R. E., Tesei, T., Thieme, M., &
739 Demouchy, S. (2021). Coseismic fault lubrication by viscous deformation. *Nature*
740 *Geoscience*, *14*(6), 437–442. https://doi.org/10.1038/s41561-021-00747-8

741 Proctor, B. P., Mitchell, T. M., Hirth, G., Goldsby, D., Zorzi, F., Platt, J. D., & Di Toro, G.
742 (2014). Dynamic weakening of serpentinite gouges and bare surfaces at seismic slip rates.
743 *Journal of Geophysical Research: Solid Earth*, *119*(11), 8107–8131.
744 https://doi.org/10.1002/2014JB011057

745 Raj, R., & Ashby, M. F. (1971). On grain boundary sliding and diffusional creep. *Metallurgical*
746 *Transactions*, *2*(4), 1113–1127. https://doi.org/10.1007/BF02664244

747 Rempel, A. W., & Weaver, S. L. (2008). A model for flash weakening by asperity melting during
748 high-speed earthquake slip. *Journal of Geophysical Research: Solid Earth*, *113*(11), 1–14.
749 https://doi.org/10.1029/2008JB005649

750 Rice, J. R. (2006). Heating and weakening of faults during earthquake slip. *Journal of*
751 *Geophysical Research: Solid Earth*, *111*(5), 1–29. https://doi.org/10.1029/2005JB004006

752 Rubino, V., Rosakis, A. J., & Lapusta, N. (2017). Understanding dynamic friction through
753 spontaneously evolving laboratory earthquakes. *Nature Communications*, *8*(May), 1–12.
754 https://doi.org/10.1038/ncomms15991

755 Schmid, S. M., Boland, J. N., & Paterson, M. S. (1977). Superplastic flow in finegrained
756 limestone. *Tectonophysics*, *43*(3–4), 257–291. https://doi.org/10.1016/0040-1951(77)90120-
757 2

758 Scholz, C. H. (2002). *The Mechanics of Earthquakes and Faulting*. *The Mechanics of*
759 *Earthquakes and Faulting*. https://doi.org/10.1017/cbo9780511818516

760 Smith, S. A. F., Di Toro, G., Kim, S., Ree, J. H., Nielsen, S., Billi, A., & Spiess, R. (2013).
761 Coseismic recrystallization during shallow earthquake slip. *Geology*, *41*(1), 63–66.
762 https://doi.org/10.1130/G33588.1

763 Sone, H., & Shimamoto, T. (2009). Frictional resistance of faults during accelerating and
764 decelerating earthquake slip. *Nature Geoscience*, *2*(10), 705–708.
765 https://doi.org/10.1038/ngeo637

766 Spagnuolo, E., Plümper, O., Violay, M., Cavallo, A., & Di Toro, G. (2015). Fast-moving
767 dislocations trigger flash weakening in carbonate-bearing faults during earthquakes.
768 *Scientific Reports*, *5*, 1–11. https://doi.org/10.1038/srep16112

769 Tinti, E., Fukuyama, E., Piatanesi, A., & Cocco, M. (2005). A kinematic source-time function
770 compatible with earthquake dynamics. *Bulletin of the Seismological Society of America*,
771 *95*(4), 1211–1223. https://doi.org/10.1785/0120040177

772 Tinti, E., Spudich, P., & Cocco, M. (2005). Earthquake fracture energy inferred from kinematic
773 rupture models on extended faults. *Journal of Geophysical Research*, *110*(B12), B12303.
774 https://doi.org/10.1029/2005JB003644

775 Di Toro, G., Han, R., Hirose, T., De Paola, N., Nielsen, S., Mizoguchi, K., et al. (2011). Fault
776 lubrication during earthquakes. *Nature*, *471*(7339), 494–499.
777 https://doi.org/10.1038/nature09838

778 Di Toro, Giulio, Goldsby, D. L., & Tullis, T. E. (2004). Friction falls towards zero in quartz rock
779 as slip velocity approaches seismic rates. *Nature*, *427*(6973), 436–439.
780 https://doi.org/10.1038/nature02249

781 Tsutsumi, A., & Shimamoto, T. (1997). High-velocity frictional properties of gabbro.
782 *Geophysical Research Letters*, *24*(6), 699–702. https://doi.org/10.1029/97GL00503

783 Viesca, R. C., & Garagash, D. I. (2018). Numerical Methods for Coupled fracture problems.
784 *Journal of the Mechanics and Physics of Solids*, *113*, 13–34.
785 https://doi.org/10.1016/j.jmps.2018.01.008

786 Violay, M., Nielsen, S., Spagnuolo, E., Cinti, D., Di Toro, G., & Di Stefano, G. (2013). Pore
787 fluid in experimental calcite-bearing faults: Abrupt weakening and geochemical signature of
788 co-seismic processes. *Earth and Planetary Science Letters*, *361*, 74–84.
789 https://doi.org/10.1016/j.epsl.2012.11.021

790 Violay, M., Passelègue, F. X., Spagnuolo, E., Di Toro, G., & Cornelio, C. (2019). Effect of water
791 and rock composition on re-strengthening of cohesive faults during the deceleration phase
792 of seismic slip pulses. *Earth and Planetary Science Letters*.

793 Yao, L., Ma, S., Platt, J. D., Niemeijer, A. R., & Shimamoto, T. (2016). The crucial role of
794 temperature in high-velocity weakening of faults: Experiments on gouge using host blocks
795 with different thermal conductivities. *Geology*, *44*(1), 63–66.
796 https://doi.org/10.1130/G37310.1

797 Yoffe, E. H. (1951). LXXV. The moving griffith crack. *Philosophical Magazine Series 7*,
798 *42*(330), 739–750. https://doi.org/10.1080/14786445108561302

799